Microchimica Acta (2020) 187: 645
https://doi.org/10.1007/s00604-020-04589-w

ORIGINAL PAPER

An electrochemical microfluidic biochip for the detection of gliadin using MoS_2/graphene/gold nanocomposite

Saipriya Ramalingam[1] · Abdallah Elsayed[1] · Ashutosh Singh[1]

Received: 16 January 2020 / Accepted: 17 September 2020 / Published online: 9 November 2020

Abstract

Testing gluten content in food, before it reaches the consumer, becomes a major challenge where cross-contamination during processing and transportation is a very common occurrence. In this study, a microfluidic electrochemical aptasensing system for the detection of gliadin has been proposed. The fabrication of the sensor involves its modification by using a combination of 2D nanomaterial molybdenum disulfide (MoS_2)/graphene with the addition of gold (Au) nanoparticles. Aptamers, a short string of nucleotide bases that are very specific to gliadin, were used in this sensor as the biomarker. The electrochemical standard reduction potential of the ferro-ferricyanide indicator was found to be ~530 mV. This setup was integrated with a unique polydimethylsiloxane (PDMS)-based flexible microfluidic device for sample enrichment and portability. The results of this sensor show that the limit of detection was 7 pM. The total sample assay time was 20 min and a good linear range was observed from 4 to 250 nM with an R^2 value of 0.982. Different flour samples sourced from the local market were tested and interfering molecules were added to ensure selectivity. The study shows promise in its applicability in real-time gliadin detection.

Keywords Gliadin · Aptasensor · 2D nanomaterials · Electrochemical biosensor · Microfluidics

Introduction

Gluten is the primary storage protein in wheat, and depending on its solubility in alcohol, it can be classified into two distinct groups: glutenin and gliadin [1]. Monomeric gliadin can be further classified as α, β, γ, and ώ-gliadins of which ώ-gliadins have the maximum amount of proline and glutamine amino acid content in them. Elevated amino acid levels in gliadin, although a rich source of protein, is also a major food allergen [2]. They are known to set off an immunoglobulin-E (Ig-E) reaction or "allergies" which exhibit themselves as asthma, severe abdominal pain, rhinitis, vomiting, urticaria, and anaphylaxis [3]. Statistics reveal that the global prevalence of gluten allergies approximately ranges between 0.5 and 1% of the total world population [4]. However, with increasing numbers of sensitive groups across the globe, food industries have looked into reducing the gluten content below the limit of allergenicity, and introducing "gluten-free" options into the market.

According to the National Institute of Health in 2004, a "gluten-free" product must include a proper label and maintain a threshold limit of gluten [5]. Countries like the USA and Canada have established that food being imported or produced must contain < 20 ppm (667 mM) of gluten ("Standards | CODEXALIMENTARIUS FAO-WHO,") [6]. However, other countries such as Japan and Australia have set their standards as 10 ppm (340 mM) and 3 ppm (100 mM) respectively [7]. Since accidental gluten ingestion can cause serious immunological reactions, it is imperative to design and develop a full-proof allergen management system that can be widely implemented. ELISA (enzyme-linked immunosorbent assay) is considered the "gold-standard" and a widely accepted technology for the detection of food allergens. The detection mechanism works on the antigen-antibody interaction and is tailored specifically for an allergen [8]. In addition to ELISA, several other techniques such as liquid chromatography-mass spectroscopy (LC-MS) [9] and polymerase chain reaction (PCR) [10] have been used to determine gluten levels in

Electronic supplementary material The online version of this article (https://doi.org/10.1007/s00604-020-04589-w) contains supplementary material, which is available to authorized users.

✉ Ashutosh Singh
asingh47@uoguelph.ca

[1] School of Engineering, University of Guelph, Guelph, ON N1G 2W1, Canada

processed foods. However, some of the major drawbacks of these techniques include multiple washing steps, longer assay time, high operational cost, low sample throughput, and inconclusive results in terms of sensitivity [11].

With the inception of biosensors in the last decade, a more specific and reliable system in the form of immunosensors were developed [12]. Of the different biosensors, electrochemical biosensors have shown promise in on-site applications due to its selectivity. Recently, transition metal dichalcogenides (2DTMD) like MoS_2 and graphene have revealed interesting properties at the nanoscale [13]. They have been since paired with biosensors to improve sensor response and sensitivity. Challenges such as cross-reactivity and false positives encountered in immunosensing gave way for the development of DNA-based recognition elements called aptamers [14]. Aptamers are a short stretch of nucleotide bases derived by SELEX (systematic evolution of ligands by exponential enrichment) process. This process incubates a gene pool with the target, allowing it to interact [15]. The elution process removes unbound primers and the bound segments are amplified, resulting in a specific sequence. Multiple trials are performed and the aptamers are rated based on their dissociation constants (K_d) [16].

In this study, the working of an integrated aptasensing system has been demonstrated for the detection of gliadin on an MoS_2/graphene/gold (MGG) nanocomposite platform. Monolayer-MoS_2 was a potential candidate for this study due to (i) increased number of active/edge-reactive sites which result in higher electron transfer rate, (ii) improved electrical conductivity due to super-lattice framework formation and electron injection, and (iii) excellent electron transfer mediation and presence of new functional groups on the surface which directly involve in electrochemical activity [17, 18]. Furthermore, the sp2 configuration of the graphene structure has proven to be an excellent candidate for electron mobility (200,000 cm^2V^{-1} s^{-1}), mechanical strength, and high stability [19]. This combination of MoS_2, graphene, and noble metal nanoparticle has been explored in this paper for its electrochemical suitability. The working electrode of this electrochemical biosensor was first modified with multiple layers of MGG nanocomposite, and initial tests were performed. A ferro-ferricyanide redox probe evaluates charge transfer characteristics between gliadin (Gli)-specific aptamer and the target. This paper also outlines the design and development of a microfluidic biochip which is integrated with the screen-printed carbon electrode (SPCE) chip. Transmission electron microscopy (TEM), X-ray diffraction (XRD), energy dispersive X-ray analysis (EDX), UV-visible spectroscopy (UV-Vis), and Raman spectroscopy were used to characterize the synthesized nanoparticles. Cyclic voltammetry (CV), differential pulse voltammetry (DPV), and electrochemical impedance spectroscopy (EIS) were used as electrochemical analysis techniques.

Experimental procedure

Materials

Molybdenum trioxide (MoO_3), hydrogen tetrachloroaurate (III) hydrate ($HAuCl_4$. $3H_2O$), graphene oxide (4 mg/ml dispersion in H_2O), potassium hexacyanoferrate ($K_4[Fe(CN)_6]$), potassium hexacyanoferrate ($K_3[Fe(CN)_6]$), N-methyl-2-pyrrolidone (NMP), phosphate-buffered saline (PBS) tablets, lysozyme (hen egg white), casein from bovine milk, and gliadin from wheat (25 g) were purchased from Millipore Sigma (Oakville, ON, Canada). Thiourea and ethanol (70%) were sourced from Fisher Scientific (Mississauga, ON, Canada). Buffers such as TE and PBS were made fresh, whenever necessary with Milli-Q water (18.2 MΩ, DI water). Screen-printed carbon electrodes (SPCEs) were acquired from Orion High Technologies (Spain). The SPCE comprises of an (Ag/AgCl) reference electrode, a 4 mm diameter working electrode, and a carbon counter electrode printed on a flexible PET substrate. SU-8 photoresists (SU-82025) and its corresponding developer solution were sourced from Microchem (Westborough, MA, USA) to prepare the master mold. PDMS (Sylgard 184) elastomer base and its curing agent were obtained from Dow Corning (Canada). The aptamer sequence specific to gliadin (Gli4) referred from previous studies [20] was synthesized and obtained from IDT Technologies (USA). To compare the results obtained for the designed biochip, Ridascreen® Gliadin R7001 ELISA kit was purchased from (Cedarlane, ON, CA). All required buffers and dilutions were prepared fresh. The aptamer (Gli4) sequence chosen is as follows:

5′-Thiol-CC AGT CTC CCG TTT ACC GCG CCT ACA CAT GTC TGA ATG CC-3′

A thiol group (-SH) was attached to the 5′ end of the aptamer to facilitate attachment to the Au nanoparticles on the synthesized MGG nanocomposite. The aptamer was obtained in a lyophilized form and suspended in TE buffer (10 mM Tris/1 mM EDTA) to prepare a stock solution of 100 μM.

Nanomaterial synthesis and characterization

MoS_2/graphene nanocomposite was prepared using a two-step hydrothermal synthesis technique followed by the growth of Au nanoparticles by citrate reduction as an adaptation form Lui et al. [21]. Briefly, MoO_3 and thiourea, in the ratio 1:5, were added to 50 ml DI and allowed to stir for 10 min. While the stirring continued for 20 more minutes, 10 mg of GO suspension was added to the mixture and later transferred to a 100-ml Teflon lined autoclave. The sealed autoclave was then placed in a hot-air oven for a period of 24 h (Fig. S1). The final black product was washed repeatedly with Milli-Q

water and centrifuging at 2000 rpm for 10 min. To prepare MGG, 0.5 g of the obtained MoS_2/graphene suspension was added to 30 ml DI and allowed to react. The temperature was increased to 90 °C and maintained for 2 h. 0.1 M of sodium citrate was added to this mixture until the solution turned pinkish-black. The MGG suspension was cooled and repeatedly washed with ethanol and water thrice before refrigeration at 4 °C for later use.

SPCE modification

To understand the basal electrode potential, unmodified screen-printed carbon electrodes (SPCE) were subject to cyclic voltammetry (CV) studies using 5 mM $[Fe(CN)_6]^{3-/4-}$. The carbon working electrode (WE) was modified by drop-casting 5 μL of the synthesized MGG nanocomposite solution. Post-modification, the electrodes were dried in a hot-air oven at 40 °C to ensure bonding between the nanocomposite and the carbon surface. The process of immobilizing the aptamer on the surface of the modified electrode is schematically represented in Fig. 1b. The lyophilized aptamer was resuspended in 1XTE buffer (pH 7.2) and 10 μL of this solution was dropped on the electrode surface. Following this, the MGG-Apt electrodes were washed with RNAse-free water to remove unbound aptamers and stored at 4 °C for further use.

Microfluidic biochip fabrication

A schematic representation of the prepared microfluidic design is given in Fig. 1a. The chip consists of two flexible PDMS layers bound to each other with the modified SPCE sandwiched between them. The channels in the microfluidic device were first designed using AutoCAD® software. The design consists of a Y-channel consisting of two inlet channels, a mixing zone, an incubation channel, and a sensing zone. This design was prepared into a photomask in the required dimension by CAD/Art Services, Inc., OR, USA. A silicon wafer was first cleaned using acetone and baked at 100 °C for 1 h and allowed to cool. Next, it was carefully mounted onto the spin chuck (Brewer Science, USA) and SU-8 negative photoresist was spin-coated. The prepared master mold was subsequently exposed to UV light (UV-KUB2) though the photomask was used to obtain the required pattern. Another round of post-exposure baking was done to improve the adhesion of desired structures.

To prepare the flexible PDMS substrate, 1 ml of curing agent was added to 10 ml of Sylgard 184, mixed, and degassed. The mixture was carefully poured over the master mold and baked for 4 h at 80 °C. The flexible PDMS substrate was separated from the mold and holes were punched to define inlet and waste collection areas. The layer comprising the SPCE (bottom layer) was made by preparing a mold of its design to give it the required depth profile. Both adhesive layers were exposed to high intensity plasma for the 40s in a vacuum environment (Harrick Plasma, PDC-32G, USA). Following surface activation, the top and bottom layers were aligned using a light microscope and bonded. Multiple modules were made to ensure repeatability and the formation of bubble-free leak proof structures.

Aptasensing of gliadin

The interaction established between Gli molecule and Gli4 aptamer determines the working principle of the proposed electrochemical biosensor. The amount of Gli4 aptamer to be immobilized on the surface of the MGG nanocomposite-

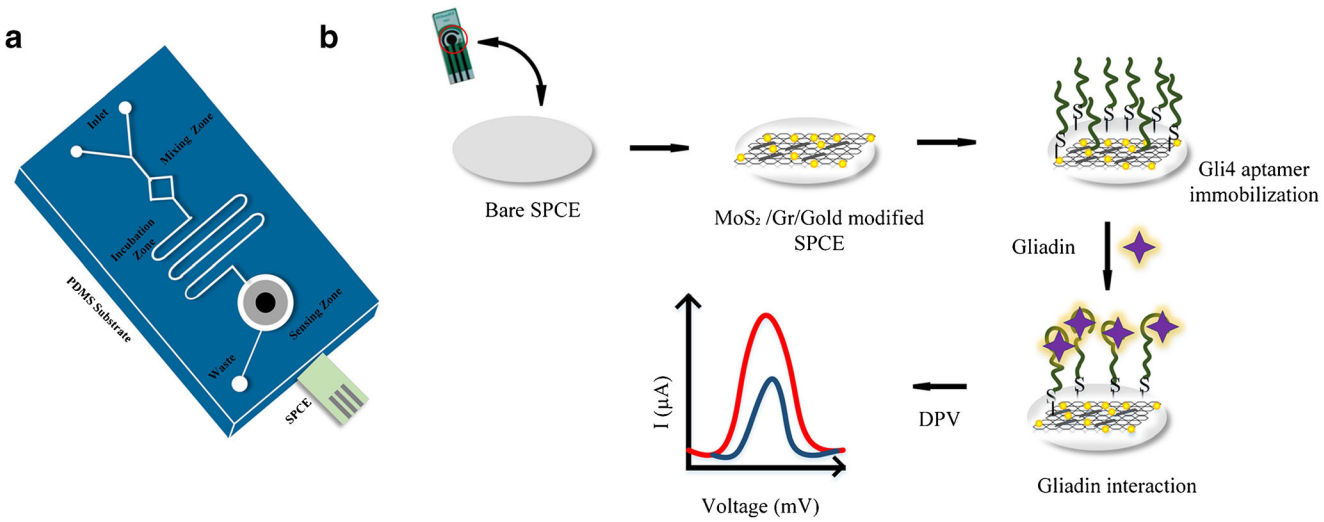

Fig. 1 Microfluidic electrochemical biochip for the detection of gliadin. (**a**) Graphical representation of the PDMS-based microfluidic chip. (**b**) Schematic of the aptamer immobilization and sensing process

modified working electrode was optimized using various concentrations and performing electrochemical studies. Once the aptamer concentration was finalized, concentrations ranging from 0.025 to 250 nM were introduced to the Gli4-modified sensor. This was incubated from periods ranging from 5 to 60 min. A known concentration of gliadin was prepared in a 1× TE buffer and introduced into the sensor through the channels. A total of 5 mM $[Fe(CN)_6]^{3-/4-}$ was injected carefully at room temperature to perform DPV studies.

An Electrochemical Potentiostat and Impedance Analyzer PalmSens® was used to test the performance of the fabricated microfluidic biochip (PalmSens4, Netherlands). Techniques such as differential pulse voltammetry (DPV) and cyclic voltammetry (CV) were used to determine the electrochemical activity of the modified sensors. The working window for CV was set from − 0.6 to 0.8 V with a constant scan rate of 0.0025 V/s. To determine the change in peak current, the derivative of LSV was used where each data point represented a current variation with voltage. DPV was conducted at an amplitude of 50 mV and a scan rate of 25 mV/s. The step potential and current range were maintained at 2 mV and 1 μA to avoid overloads. The sensor end of the microfluidic system was attached to the connector on the potentiostat for analysis.

Real sample preparation

Different flour samples were purchased from a local grocery store from the "gluten-free" section. Ethanolic extraction was used to extract gliadin from different flour samples. The flour was first suspended in water in the ratio 1:10 and constantly shaken for 2 h. Furthermore, this suspension was centrifuged at 6000 rpm for 10 min. The pellet was isolated and the supernatant was discarded. The collected pellet was resuspended in 60% ethanol, in the ratio 1:5, and shaken for 1 h. This suspension was again subject to centrifugation at 5000 rpm for 20 min to extract gliadin. The supernatant was collected and transferred into a fresh centrifuge tube as a stock solution. Five hundred microliters of the stock solution was resuspended in 1× TE buffer and stored at 6 °C.

Results and discussion

Nanomaterial synthesis and electrode modification

The properties of 2D nanosheets have always triggered the interest of researchers over the years, and in this paper, a combination of 2 layered materials have been used. The synthesis of MoS_2–graphene nanocomposite was performed to evaluate the characteristic of electron conductivity between the two layered materials. Recent studies on 2D hetero-conjugates have shown the existence of a synergistic effect between the bilayers. Near-zero band gap behavior was achieved and different stacking configurations affect Fermi level shifts [22]. Defects and vacancies formed on the surface of the MoS_2-graphene interface have shown higher electron transfer rates by computational studies. However, its application in the field of biosensing has not been explored as much as in Na^{2+} ion batteries [23]. In this research, a two-step hydrothermal synthesis technique was used to prepare MGG nanostructures. The formation of these structures was confirmed successfully using various non-characterization techniques. Morphological characteristics were first evaluated using TEM where a small drop of dilute MGG and MoS_2/graphene nanocomposite (0.5 mg/ml) was dropped on a gold-doped copper grid (Fig. 3A). Rolled up sheets of MoS_2 were observed on the surface of graphene at 50 nm magnification. The temperature and pressure parameters in addition to reducing agent thiourea converted graphene oxide into graphene sheets. Aggregation of MoS_2 on the surface of graphene was absent over a wide range of areas. In the bulk state, MoS_2 assumes a thermodynamically favorable S-Mo-S, 2H polymorphic state. The chemical exfoliation process allows the bulk MoS_2 to increase its active sites through edge properties, thus improving reactivity [24]. On the other hand, GO is an electrically insulating material due to its thickly packed structure. By way of chemical reduction, GO can be reduced to near-graphene or "reduced-graphene oxide"-like state which will restore its conductivity by the inclusion of a π-bonding network between the layers [25]. The oxidation process itself breaks the bond between the graphitic structures removing oxygen functionality in the lattice. In the case of Au nanoparticle growth of MoS_2/graphene, citrate reduction was the primary, shape, and size controlling step. Citrate had a dual effect on MoS_2/graphene nanocomposite mesh as it was responsible for both nucleation of Au^{3+} and also stabilizing the structures [26]. The thiol group present at the 5′ end of the aptamer has the highest affinity to Au nanoparticles. This property of SH-Au binding circumvents the use of a carbodiimide cross-linker molecule such as EDC-NHS. Hence, the number of modification steps is reduced and the attachment of the aptamer to the surface of the electrode is successful. For accurate characterization purposes, gold nanoparticles were separately synthesized and TEM was performed (Fig. 2). The size of the Au nanoparticles was determined to be approximated to 8 nm using an image processing software, ImageJ. TEM of MGG nanocomposites revealed a near-even distribution of Au nanoparticles over the surface of MoS_2/graphene and the attachment of Au nanoparticles on its sheet-like surface. The gold nanoparticles exhibited a characteristic Vis-absorbance peak at 550 nm confirming its formation (Fig. 2b).

Elemental analysis (EDX) on both MoS_2/graphene nanocomposite and MGG nanocomposite w**as** performed to understand the extent of Au nanoparticle formation on the MoS2/graphene. The modified working electrode of the SPCE was analyzed for its elemental composition at various points. Figure 3b shows carbon, oxygen, molybdenum, and

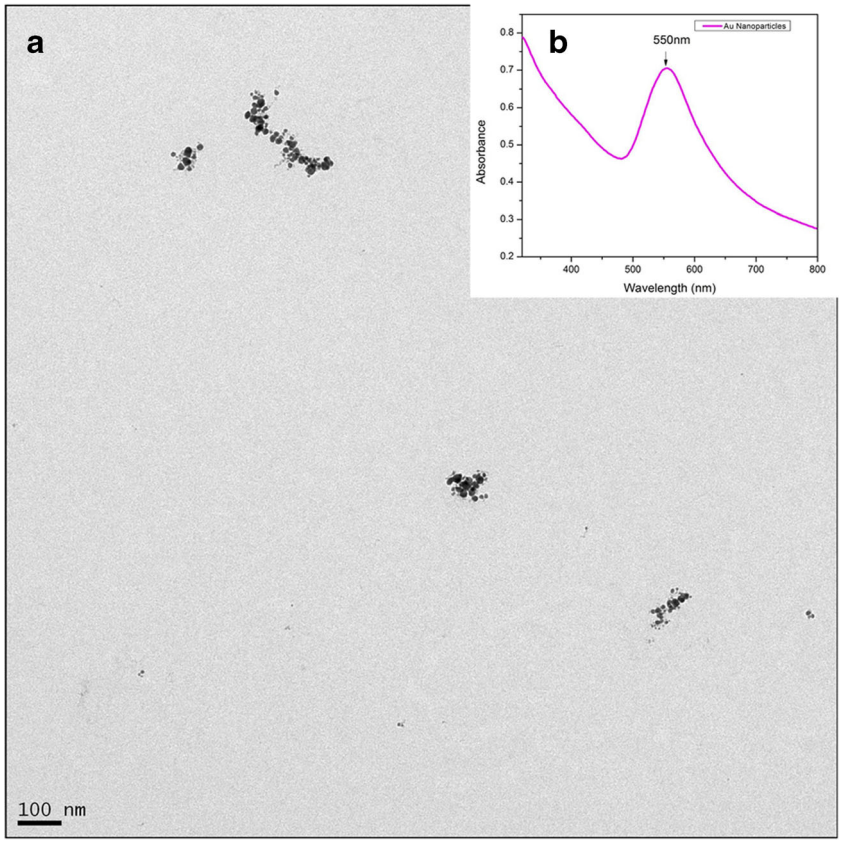

Fig. 2 TEM of Au nanoparticles (inset: UV-Vis spectra)

sulfur content, as expected, in the synthesized MoS_2/graphene nanocomposite. MGG nanocomposites, on the other hand, showed the presence of Au nanoparticles. This Au nanoparticle formation can be attributed to an increased edge- activity of MoS_2 and graphene sheets [27]. Different EDX analysis points not only confirmed the presence of MGG nanocomposites but also even distribution on the electrode surface.

Raman spectroscopy was performed on the synthesized MoS_2/graphene and MGG nanocomposites to determine their atomic structure. A 532-nm laser was used with a total power of 20 mW. Ten accumulations were run for a period of 2 s for (a) MoS_2, (b) GO, (c) MoS_2-graphene, and (d) MGG nanocomposite (Fig. S2). MoS_2 exhibited Raman fingerprint by its characteristic peaks at 384.2 cm^{-1} and 408.7 cm^{-1} [28]. In-plane E^1_{2g} vibrational mode was observed at 384.2 cm^{-1} and out-of-plane A^1_g vibrational mode at 408.7 cm^{-1}. It has been established in earlier studies that the intensity of A^1_g vibrational mode increases with an increase in the number of monolayers as the subsequent in-plane E^1_{2g} vibrational mode intensity decreases. Although this was not experimentally calculated, it can be observed in the Raman spectrum of MGG nanocomposite that the intensity of E^1_{2g} has significantly reduced. Raman spectra of GO has been extensively studied over the years [29]. The D and G bands are the most predominant vibrational modes which represent disorder and stacking in graphitic structures. The ratio of the intensities of D/G determines the extent of exfoliation. In the GO response curve, D/G ratios are higher compared to MoS_2/graphene (lower) or MGG nanocomposites (least) which point to the fact that GO has been reduced and the number of exfoliated layers are significantly lower. The blue shift of the G band can also act as a confirmatory test for the formation of reduced graphene oxide or near graphite-like entities [30].

Also, Au nanoparticles exhibited significant surface-enhanced Raman scattering (SERS) around 1110 cm^{-1}, masking the peaks corresponding to MoS_2 and graphene. X-ray diffraction patters of the prepared nanomaterials were analyzed using Philips PW1830 X-ray Diffractometer with a Cu-Kα source. Figure S3 (A) depicts the XRD pattern of MoS_2-graphene nanocomposite where the (002) peak exhibits broadening compared to pristine MoS_2 which are corroborated by PDF cards 771716. This indicates that (i) the layered crystallinity of MoS_2 remained intact through the hydrothermal synthesis process and (ii) intermediate GO moieties can act as a potential nucleation site for the formation of MoS_2 sheets. The (002) plane growth of MoS_2 was significantly retarded by the inclusion of graphene. This, in turn, inhibited the restacking of graphene, during the hydrothermal process [17]. The very small concentration of graphene (2%) included during synthesis could be the reason for not observing significant

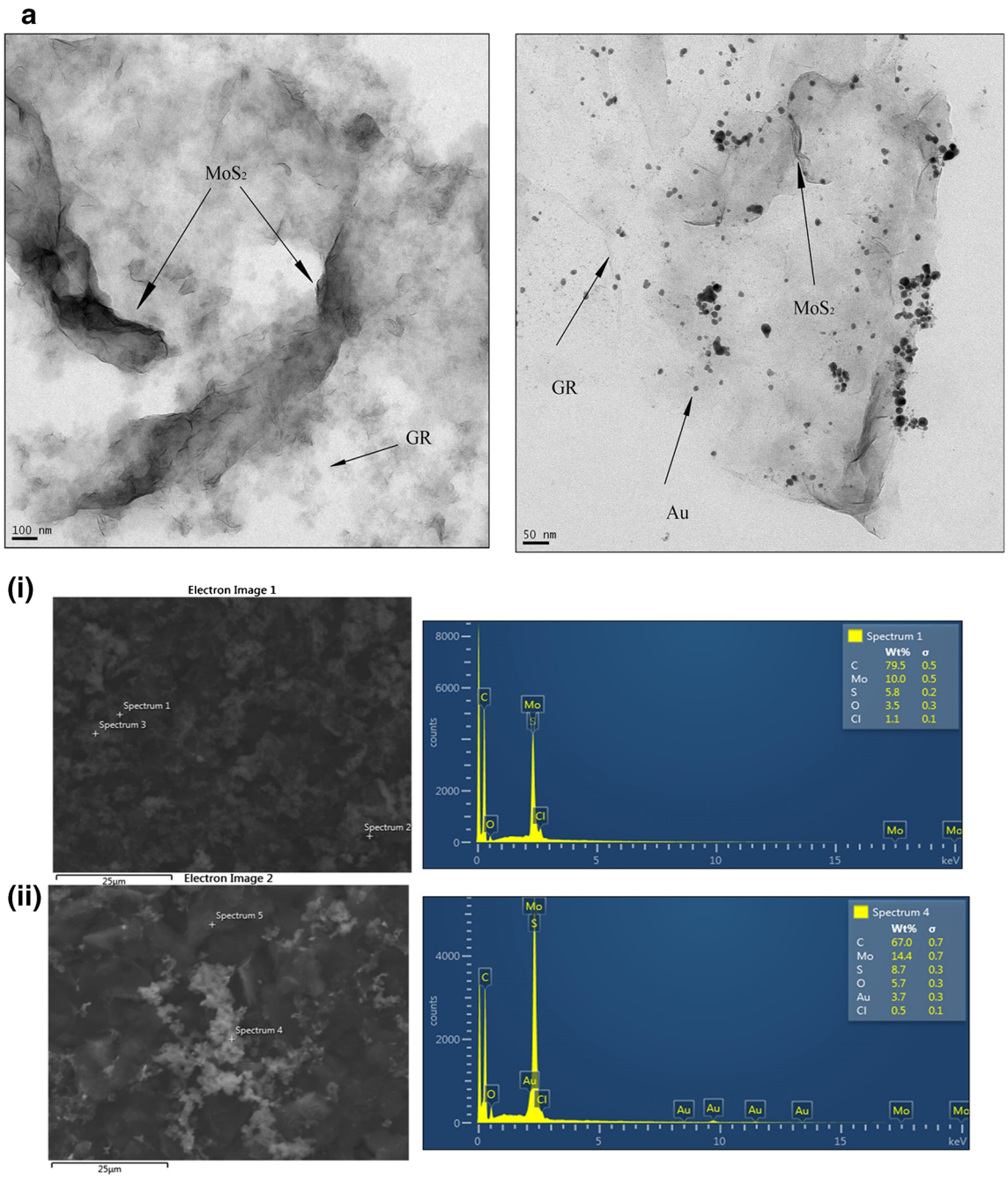

Fig. 3 (**a**) TEM of MoS_2/graphene and MoS_2/graphene/gold nanocomposite. (**b**) SEM images with corresponding EDX data of (i) MoS_2/graphene sheets and (ii) MoS_2/graphene/gold nanocomposites

characteristic peaks. Characteristic gold peaks were observed in the XRD patters of MGG nanocomposite shown in Fig. 3B. The Au pattern matches well with the JCPDS file: 04-0784 where peaks such as (111), (002), (022), and (113) were prominent among MG nanocomposite peaks (Fig. S3(B)).

Following morphological and structural characterization, electrochemical studies were performed. Bare carbon electrodes did not show any significant current on analysis using 5 mM $[Fe(CN)_6]^{3-/4-}$ as the redox pair. As shown in Fig. S4 (i), different modifications (of equal concentration) were made to clean, bare SPCEs, and their corresponding peak currents were measured. The number of layers per each modification was kept constant for all analyses. MoS_2 and GO showed good electrochemical activity compared to the bare electrode, but MGG nanocomposites gave the highest peak current. This can be attributed to the improved electron transfer kinetics between MoS_2 and graphene nanostructures. An increase in anodic and cathodic peak current can be attributed to the synergistic effect between MoS_2, graphene, and gold nanoparticles. The growth of Au nanoparticles was assisted by the

porous nature of MoS_2 and sheet-like structure of graphene, improving the charge carrier flow through the lattice. Scan rate dependency studies were also performed on the modified electrodes to ensure its stability as shown in Fig. S4 (ii). The scan rate was varied from 10 to 200 mV/s using 100 μL 5 mM $[Fe(CN)_6]^{3-/4-}$ as the redox indicator. The consistent increase in peak current with scan rate and absence of peripheral peaks can be indicative of sensor stability. A 3-layer modification was necessary for successful adhesion of MGG nanocomposite to the electrode surface.

Electrochemical impedance spectroscopy was performed to determine the behavior of each modified layer to the final nanocomposite arrangement. Similar to CV and DPV studies, 5 mM $[Fe(CN)_6]^{3-/4-}$ was used as a redox probe for analysis. Figure S5 represents the Nyquist plots obtained for (i) bare electrode, (ii) bulk MoS_2, (iii) MG nanocomposite, and (iv) MGG nanocomposites on screen-printed carbon electrodes. The bare electrode had the highest semicircle radius which can be conclusive of high charge transfer resistance (R_{ct}). Least charge transfer resistance was observed in the MGG nanocomposite configuration, which indicated that the electron movement between the layers became very easy as the repulsion between the $[Fe(CN)_6]^{3-/4-}$ ions decreased. The experimental data observed was fitted into the Randles circuit, given by $[R_s(C_{dl}[R_{ct}\ Z_w])]$ (Fig. S5, inset). Here, the solution resistance is given by R_s, while R_{ct} represents the charge transfer resistance, Z_w is the Warburg impedance component and C_{dl} is the corresponding double-layer capacitance. The developed equivalent circuit gave the following values R_s 786.8 Ω, R_{ct} 0.074 Ω, Z_w 5.704KΩ, and C_{dl} 3.913 μF after 10 iterations. The observed EIS results were corroborated by the DPV and CV responses, and hence, a concentration of 1 mg/ml MGG was used for further experiments.

Sensor optimization

The principle of self-assembly allows DNA and alike structures to follow molecular order on the surface of Au nanoparticles. Thiol and dithiol SAMs are known to adhere to Au (111), exposing their terminal group for further linkages. The interaction of Gli4 was performed in a liquid suspension of 100 μL, just sufficient to cover the working electrode surface. The following parameters were optimized for this experiment: (i) Aptamer concentration: varying concentrations from 0.25 to 2 μM while maintaining the incubation period for 8 h at 6 °C was tested on various SPCEs. Next, 100 μL of 5 mM $[Fe(CN)_6]^{3-/4-}$ was used to run DPV analyses and the maximum peak current was observed at 1 μM concentration. Increasing concentrations of aptamers on the surface of the electrode showed retarded electron kinetics as observed in Fig. 4a. (ii) Aptamer interaction time: interaction time between gliadin protein and Gli-Apt was varied from 5 to 60 min to study the change in peak current. 0.5 μM of the target was allowed to interact with Gli4 aptamer on the sensor surface (Fig. 4b). After each incubation period, 5 mM $[Fe(CN)_6]^{3-/4-}$ was used to run DPV analyses. The highest peak current was achieved at 10 min and a significant decreasing trend was observed with increasing time. Observing the current trend, a 10-min window was used for further analyses. A pH of 7.5 was maintained throughout the experiment.

Microfluidic biochip fabrication and integration

Scaling down the size and improving portability, while reducing the occurrence of false positives was the objective of a lab-on-chip design. The point-of-care system acts as a durable yet flexible platform for the assay. PDMS-based soft lithographic technique has been one of the simplest ways to prepare a microfluidic channel. The aspect of micro-manipulation has given rise to μ-TAS (micro-total analysis systems) which can perform multiple tasks on a single platform. In this study, the microfluidic chip was used to facilitate sample flow, improve sensitivity, and reduce sample usage. Dimensions of the biochip were carefully altered according to need. Briefly, the width of each channel was set to 75 μm, and the sample collection chambers had a depth of 2 mm and a diameter of 2 mm. The design of the chip comprised two sample inlets, one for the aptamer solution and the other for the Gli sample. A depression similar to the dimensions of the working electrode was made for the sample to be collected on the working electrode surface.

One of the challenging aspects of the sensor is to ensure the development of the structures on the Si wafer. Furthermore, the deposition of PDMS on the developed Si wafer can introduce air bubbles if not handled with care. This continuous-flow device allowed the sample to be mixed, incubated, and analyzed. As depicted in Fig. 5, the microfluidic-SPCE was attached to the PalmSens® potentiostat. The micro-tubing extensions were used to pump the samples manually using a 1-ml injection. Care was taken to ensure experiments were performed in a cleanroom to avoid dust from settling on to the chip. Next, 100 μL of 5 mM $[Fe(CN)_6]^{3-/4-}$ was used to perform DPV studies to determine peak current. The interaction of the Gli sample with Gli4 aptamer resulted in a reduction in peak current with increasing concentrations of Gli.

Different concentrations of pure wheat gliadin samples were introduced into the aptamer-modified sensor to determine its overall sensitivity. A range of 25 pM–250 nM concentrations were suspended in a 1× TE buffer. As shown in Fig. 6a, a change in cathodic peak current was observed with blank ranging close to 8.126 μA. When higher concentrations like 250 nM were studied, a current dropped to 1.5 μA. The Gli4 aptamer undergoes a conformational change as it has the highest affinity towards the incoming gliadin sample, due to its low dissociation factor.

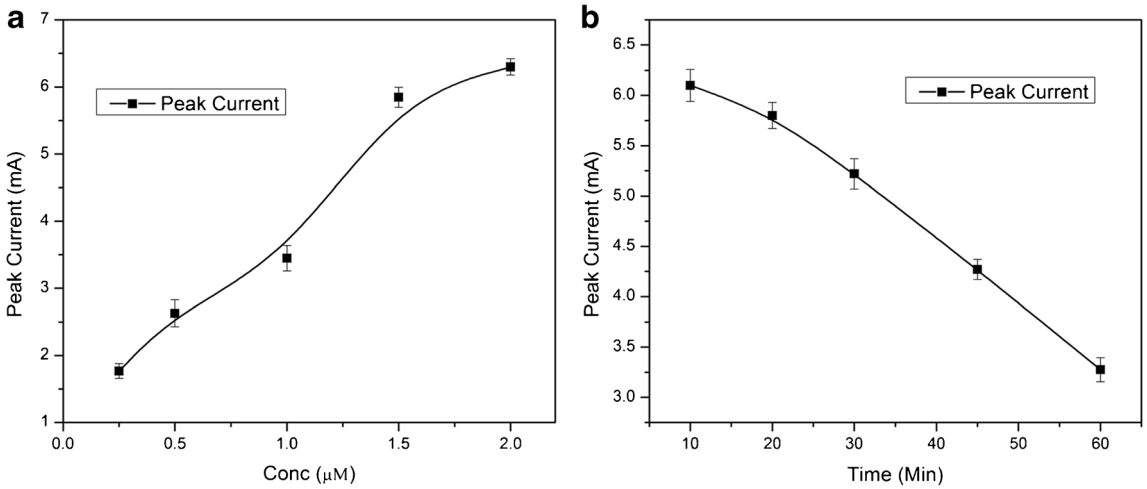

Fig. 4 Optimization of gliadin sensor. (**a**) Plots of peak currents from DPV signals obtained from various aptamer concentrations. (**b**) Time-dependent change in peak current between Gli-Apt and gliadin target in the presence of 5 mM $[Fe(CN)_6]^{3-/4-}$

This restricts the activity of potassium ferro-ferricyanide on the surface of the electrode, hence reducing peak current. The experiments were repeated in triplicates to confirm the observed results. The peak currents were plot as a graph of peak anodic current (I_{pa}) on the Y-axis and corresponding gliadin concentrations were used on the X-axis. The linear range of the sensor was observed from 4 to 250 nM and a linear fitting model was developed in Fig. 6b. The linear equation of y = 5.5196–0.0185x was derived from the linear graph and the correlation coefficient

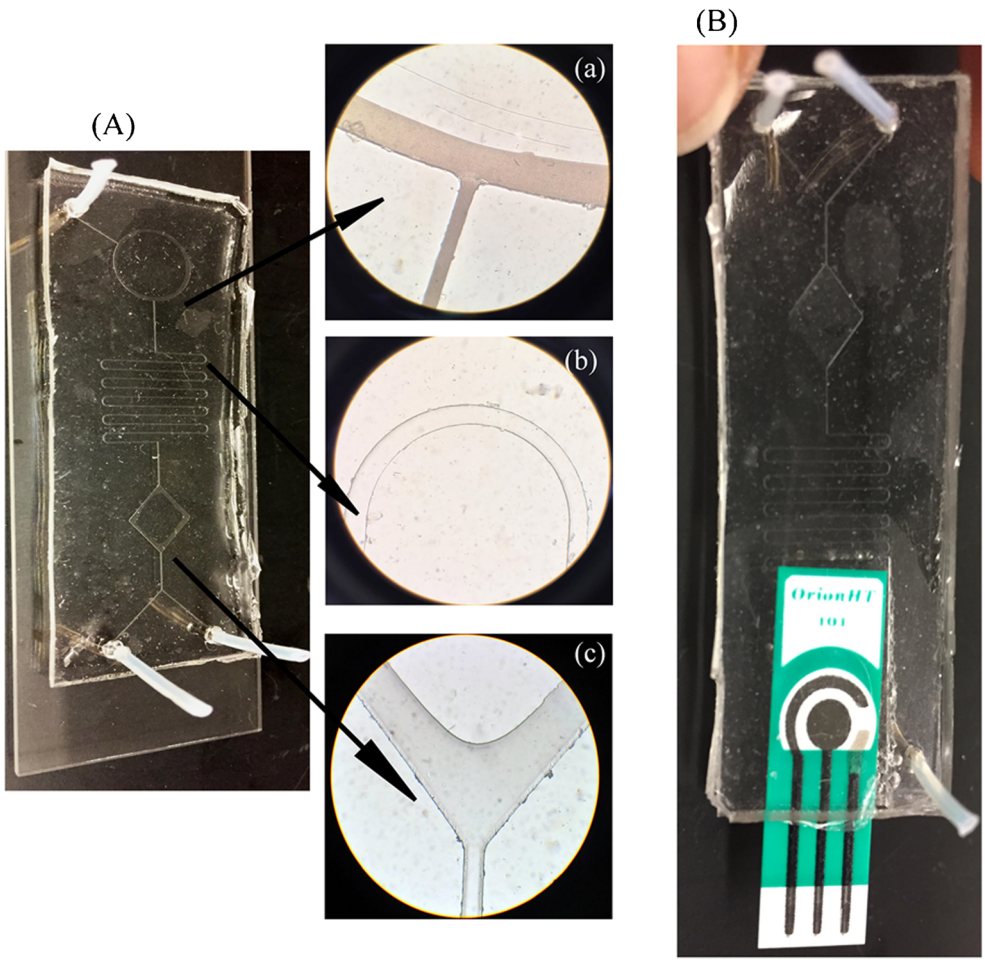

Fig. 5 (A) Photograph for the prepared PDMS microfluidic biochip at × 20 magnification: (a) Channel design connecting to working electrode. (b) Incubation chambers. (c) Mixing channel. (B) Prototype of the final sensor

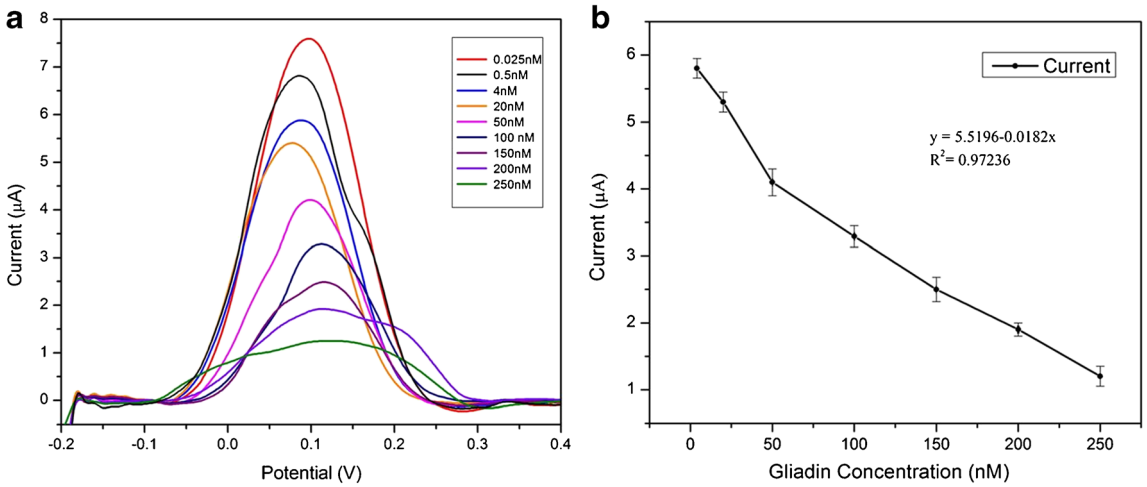

Fig. 6 Gliadin aptasensing. (A) DPV signals obtained for various test concentrations of gliadin. (B) Linear range obtained from the peak currents obtained for various concentrations of gliadin interactions (inset). Linear range 4–250 nM with an $R^2 = 0.97236$

was $R^2 = 0.982$. The limit of detection of the sensor was calculated to be 7 pM using the formula (3*σ)/slope.

Selectivity and stability

Selectivity is one of the most important aspects in determining the viability of a sensor in real-time applications. The idea of an apta-microfluidic biochip integrated with a screen-printed carbon electrode was to reduce the occurrence of false positives. Since the idea of sensor application was more intended towards the food industry, negative control studies were performed. Rice flour, known to be naturally "gluten-free" was chosen for spiking with pure wheat gluten. Table 1 displays the results of the spike test, indicating that a good recovery was observed between 98 and 102%.

An average of 3 trials gave an error range between 0.5 and 2%. Next, different interfering molecules were introduced onto the working electrode surface such as hen egg lysozyme, casein, chickpea flour, rice flour, and corn flour (Fig. 7a). Equal concentrations of each (200 nM) were introduced onto the modified sensor surface. The mixture was incubated for 20 min and analyzed by DPV using 100 μL of 5 mM $[Fe(CN)_6]^{3-/4-}$. Anodic peak currents were plotted in the form of a bar graph for ease in the analysis. Results showed chickpea flour, casein, and hen egg lysozyme to have more than or equal to blank. No significant interaction was observed.

Table 1 Detection of gliadin from spiked rice flour by microfluidic biochip

Spiked concentration (pM)	Detected concentration (pM)	% Recovery
5	6.19	120.80
40	42.05	104.75
100	101.66	101.51
500	504.012	100.78
1000	998.51	99.83

Furthermore, items in the "gluten-free" section of a local store were tested for its gliadin content. The preparation of the samples was as explained in the "Real sample preparation" section. Figure 7b depicts the concentration of gliadin present in samples per the linear graph developed for this sensor. Similar to previous experiments, DPV measurements were taken and $n = 3$ replicates were made for each trial for statistical significance. Coconut flour, all-purpose baking flour, and white rice powder had gluten levels less than 6 ppb, which is way below the stipulated guidelines for "gluten-free" items. When normal wheat flour was tested against the sensor, very low current ($I_{pa} = 0.35$ μA) was observed which puts the range of gliadin above 1000 nM. This shows that the sensor was able to detect a wide range of "gluten-free" and gluten-containing food products.

The sensitivity of the as-prepared sensor was evaluated against a commercial kit. Ridascreen ® Sandwich immunoassay was performed for samples spiked with gluten, following the procedure indicated in the kit. Sample extraction for ELISA required a two-step process using a patented cocktail solution. Briefly, 0.25 ml of the sample was added to ×10 times the amount of cocktail patented and incubated. Following a 40-min incubation time, the sample was added to 7.5 ml of 80% ethanol and shaken for 1 h. This mixture was further centrifuged at 2500*g* and the supernatant was transferred into given buffer dilutions. Recovery percentage was calculated as follows:

$$\text{Recovery}(\%) = \left(C'' - Cb\right)/Cs$$

where C″ is the mean gliadin concentration obtained for the spiked samples. C_b is the mean gliadin concentration

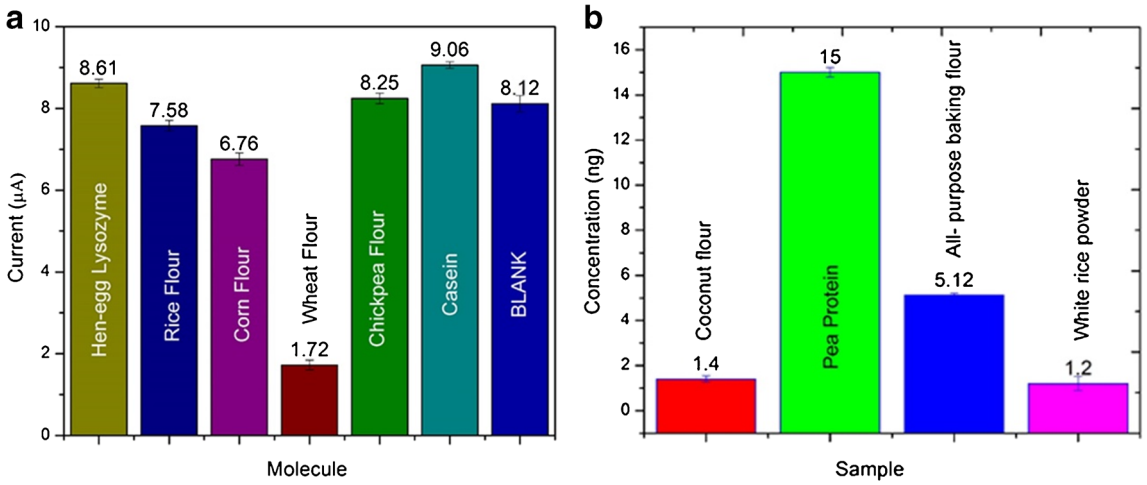

Fig. 7 (**a**) Interaction between Gli-aptamer with equal concentration (200 nM). Hen egg lysozyme, rice flour, corn flour, wheat flour, chickpea flour, and casein ($n = 3$). (**b**) Sample flours labeled "gluten-free" in the local grocery store: (a) coconut flour, (b) pea protein, (c) all-purpose baking flour, (d) white rice flour ($n = 3$)

of blank and C_s is the known concentration of gliadin spiked into the sample. Results obtained from the biochip align well with that of a commercial ELISA kit shown in Table 2. Stability is an important parameter to test, which is a yardstick of the sensor's performance in real-time. Long-term stability studies were performed by storing modified microfluidic electrochemical biosensors for 60 days at 4 °C. Sensors were evaluated every 10 days by introducing 0.5 nM gliadin to the surface, while using 5 mM $[Fe(CN)_6]^{3-/4-}$ as a redox indicator. The first 3 weeks gave a peak current within the error range, while a deviation of 3.5% was recorded in weeks 4 and 5 (Fig. S6). Although the sample preparation time is comparable, the number of incubation and washing steps in the proposed biochip has been significantly reduced. The drawback of this biosensor could be its inability to detect high concentrations (in the range of mM), due to saturation on the electrode surface. Also, the assembly of this sensor in a microfluidic casing would be tricky and requires technical precision and a cleanroom facility. The performance of this aptasensor was compared to recently published literature, collated in Table S1.

Conclusion

This study highlights the importance of food safety by the design and fabrication of a microfluidic point-of-care device for gliadin detection. As proof of concept, an electrochemical detection system was studied. The use of two very widely used 2D TMD's showed the synergistic effect of electron transfer through the working electrode. Gold nanoparticles not only provide overall stability to the system but also formed a platform for the aptamer to attach itself through –SH bonding. This reduced the number of functionalization steps making it easy for fabrication. To further simplify the system and improve portability, a PDMS-based microfluidic chip was designed. The size characteristics allowed the sample to be filtered, mixed, and incubated within the chip, thus improving sensitivity. No significant cross-reactivity was observed in this study which tested various gluten-free foods for its levels. This sensor finds its application as a point-of-care device for efficient on-field testing of gliadin in the food safety sector.

Funding The authors sincerely thank the Natural Sciences and Engineering Research Council of Canada (NSERC) for funding this study (Grant # RGPIN-2017-03975). The authors would also like to acknowledge the OMAFRA-U of G Partnership (Ontario Ministry of Agriculture,

Table 2 Detection of gliadin from spiked samples in food samples using ELISA

Spiked concentration (ng/ml)	Detected concentration of biosensor (ng/ml)	% Recovery of biosensor	Detected concentration by ELISA kit (ng/ml)	% Recovery of ELISA kit
6.00	7.20	117.5	5.64 ± 0.02	91.5
15.00	16.45	108.67	12.89 ± 0.05	84.933
30.00	28.96	96.03	32.11 ± 0.1	106.533
60.00	62.68	104.21	58.44 ± 0.05	97.15
80.00	79.14	98.73	81.09 ± 0.04	101.175

Food and Rural Affairs) for funding this study through their Highly Qualified Personnel (HQP) Scholarship Program.

Compliance with ethical standards

Conflict of interest The authors declare that they have no competing interest.

References

1. Wieser H (2007) Chemistry of gluten proteins. Food Microbiol 24: 115–119. https://doi.org/10.1016/J.FM.2006.07.004
2. Singh A, Munshi S, Raghavan V et al (2013) Effect of external electric field stress on gliadin protein conformation. Proteomes 1: 25–39. https://doi.org/10.3390/proteomes1020025
3. Inomata N (2009) Wheat allergy. Curr Opin Allergy Clin Immunol 9:238–243. https://doi.org/10.1097/ACI.0b013e32832aa5bc
4. Leonard MM, Vasagar B (2014) US perspective on gluten-related diseases. Clin Exp Gastroenterol 7:25–37. https://doi.org/10.2147/CEG.S54567
5. Cianferoni A (2016) Wheat allergy: diagnosis and management. J Asthma Allergy 9:13–25. https://doi.org/10.2147/JAA.S81550
6. Standards | CODEXALIMENTARIUS FAO-WHO. http://www.fao.org/fao-who-codexalimentarius/codex-texts/list-standards/en/. Accessed 27 Jun 2019
7. Kagan RS (2003) Food allergy: an overview. Environ Health Perspect 111:223–225. https://doi.org/10.1289/ehp.5702
8. Diaz-Amigo C, Popping B (2013) Accuracy of ELISA detection methods for gluten and reference materials: a realistic assessment. J Agric Food Chem 61:5681–5688. https://doi.org/10.1021/jf3046736
9. Lock S, Lock S (2013) Gluten detection and speciation by liquid chromatography mass spectrometry (LC-MS/MS). Foods 3:13–29. https://doi.org/10.3390/foods3010013
10. Allmann M, Candrian U, Hefelein C, Lthy J (1993) Polymerase chain reaction (PCR): a possible alternative to immunochemical methods assuring safety and quality of food detection of wheat contamination in non-wheat food products. Zeitschrift fr Leb Forsch 196:248–251. https://doi.org/10.1007/BF01202741
11. Weng X, Neethirajan S (2016) A microfluidic biosensor using graphene oxide and aptamer-functionalized quantum dots for peanut allergen detection. Biosens Bioelectron 85:649–656. https://doi.org/10.1016/J.BIOS.2016.05.072
12. Ronkainen NJ, Halsall HB, Heineman WR (2010) Electrochemical biosensors. Chem Soc Rev 39:1747–1763. https://doi.org/10.1039/b714449k
13. Alarcon-Angeles G, Álvarez-Romero GA, Merkoçi A (2016) Emerging nanomaterials for analytical detection. Compr Anal Chem 74:195–246. https://doi.org/10.1016/bs.coac.2016.03.022
14. Acquah C, Agyei D, Monney I et al (2018) Aptameric sensing in food safety. Elsevier Inc.
15. Sharma R, Ragavan KV, Thakur MS, Raghavarao KSMS (2015) Recent advances in nanoparticle based aptasensors for food contaminants. Biosens Bioelectron 74:612–627. https://doi.org/10.1016/j.bios.2015.07.017
16. Wu YX, Kwon YJ (2016) Aptamers: the "evolution" of SELEX. Methods 106:21–28. https://doi.org/10.1016/J.YMETH.2016.04.020
17. Chang K, Chen W (2011) In situ synthesis of MoS2/graphene nanosheet composites with extraordinarily high electrochemical performance for lithium ion batteries. Chem Commun 47:4252–4254. https://doi.org/10.1039/c1cc10631g
18. Zheng X, Xu J, Yan K, Wang H, Wang Z, Yang S (2014) Space-confined growth of MoS2 nanosheets within graphite: the layered hybrid of MoS2 and graphene as an active catalyst for hydrogen evolution reaction. Chem Mater 26:2344–2353. https://doi.org/10.1021/cm500347r
19. Stankovich S, Dikin DA, Piner RD, Kohlhaas KA, Kleinhammes A, Jia Y, Wu Y, Nguyen SBT, Ruoff RS (2007) Synthesis of graphene-based nanosheets via chemical reduction of exfoliated graphite oxide. Carbon N Y 45:1558–1565. https://doi.org/10.1016/J.CARBON.2007.02.034
20. Amaya-González S, López-López L, Miranda-Castro R, de-los-Santos-Álvarez N, Miranda-Ordieres AJ, Lobo-Castañón MJ (2015) Affinity of aptamers binding 33-mer gliadin peptide and gluten proteins: influence of immobilization and labeling tags. Anal Chim Acta 873:63–70. https://doi.org/10.1016/J.ACA.2015.02.053
21. Liu H, Chen X, Deng L, Su X, Guo K, Zhu Z (2016) Preparation of ultrathin 2D MoS2/graphene heterostructure assembled foam-like structure with enhanced electrochemical performance for lithium-ion batteries. Electrochim Acta 206:184–191. https://doi.org/10.1016/j.electacta.2016.04.160
22. Xie X, Ao Z, Su D, Zhang J, Wang G (2015) MoS2/graphene composite anodes with enhanced performance for sodium-ion batteries: the role of the two-dimensional heterointerface. Adv Funct Mater 25:1393–1403. https://doi.org/10.1002/adfm.201404078
23. David L, Bhandavat R, Singh G (2014) MoS2/graphene composite paper for sodium-ion battery electrodes. ACS Nano 8:1759–1770. https://doi.org/10.1021/nn406156b
24. Wang K, Wang J, Fan J, et al (2013) Ultrafast saturable absorption of two-dimensional MoS 2 nanosheets. https://doi.org/10.1021/nn403886t
25. Zhu Y, Murali S, Cai W, Li X, Suk JW, Potts JR, Ruoff RS (2010) Graphene and graphene oxide: synthesis, properties, and applications. Adv Mater 22:3906–3924. https://doi.org/10.1002/adma.201001068
26. Ji X, Song X, Li J, et al (2007) Size control of gold nanocrystals in citrate reduction: the third role of citrate. https://doi.org/10.1021/ja074447k
27. Yu X, Shiraki T, Yang S, Ding B, Nakashima N (2015) Synthesis of porous gold nanoparticle/MoS $_2$ nanocomposites based on redox reactions. RSC Adv 5:86558–86563. https://doi.org/10.1039/C5RA15421A
28. Chhowalla M, Shin HS, Eda G, Li LJ, Loh KP, Zhang H (2013) The chemistry of two-dimensional layered transition metal dichalcogenide nanosheets. Nat Chem 5:263–275. https://doi.org/10.1038/nchem.1589
29. Kudin KN, Ozbas B, Schniepp HC et al (2007) Raman spectra of graphite oxide and functionalized graphene sheets. NanoLetters 8: 36–41. https://doi.org/10.1021/NL071822Y
30. Wang G, Yang J, Park J, Gou X, Wang B, Liu H, Yao J (2008) Facile synthesis and characterization of graphene nanosheets. J Phys Chem C 112:8192–8195. https://doi.org/10.1021/jp710931h